



**HAL**  
open science

# Two-dimensional heat transfer coefficients with simultaneous flow visualisations during two-phase flow boiling in a PDMS microchannel

Sofia Korniliou, Coinneach Mackenzie-Dover, John R.E. Christy, Souad Harmand, Anthony J. Walton, Khellil Sefiane

► **To cite this version:**

Sofia Korniliou, Coinneach Mackenzie-Dover, John R.E. Christy, Souad Harmand, Anthony J. Walton, et al.. Two-dimensional heat transfer coefficients with simultaneous flow visualisations during two-phase flow boiling in a PDMS microchannel. *Applied Thermal Engineering*, 2018, 130, pp.624-636. 10.1016/j.applthermaleng.2017.11.003 . hal-03450056

**HAL Id: hal-03450056**

**<https://uphf.hal.science/hal-03450056>**

Submitted on 23 May 2022

**HAL** is a multi-disciplinary open access archive for the deposit and dissemination of scientific research documents, whether they are published or not. The documents may come from teaching and research institutions in France or abroad, or from public or private research centers.

L'archive ouverte pluridisciplinaire **HAL**, est destinée au dépôt et à la diffusion de documents scientifiques de niveau recherche, publiés ou non, émanant des établissements d'enseignement et de recherche français ou étrangers, des laboratoires publics ou privés.



Distributed under a Creative Commons Attribution - NonCommercial - NoDerivatives 4.0 International License

# TWO-DIMENSIONAL HEAT TRANSFER COEFFICIENTS WITH SIMULTANEOUS FLOW VISUALISATIONS DURING TWO-PHASE FLOW BOILING IN A PDMS MICROCHANNEL

S.Korniliou<sup>c,d\*</sup>, C. Mackenzie Dover<sup>b</sup>, J.R.Christy<sup>d</sup>, S.Harmand<sup>c</sup>, A.J.Walton<sup>b</sup>, K.Sefiane<sup>a,d</sup>

<sup>a</sup> *Tianjin Key Lab of Refrigeration Technology, Tianjin University of Commerce, Tianjin City 300134, PR China*

<sup>b</sup> *Institute for Micro and Nano Systems, School of Engineering, SMC, Alexander Crum Brown Road, Edinburgh, EH9 3FF, UK*

<sup>c</sup> *UVHC, LAMIH/ CNRS8201, Valenciennes 59313, France*

<sup>d</sup> *Institute for Multiscale Thermofluids, School of Engineering, University of Edinburgh, King's Buildings, Colin Maclaurin Road, Edinburgh, EH9 3DW, UK*

\*Corresponding author: Fax: +33(0)327 511578 Email: S.Korniliou @ed.ac.uk

## ABSTRACT

Infrared (IR) thermography was combined with simultaneous high speed flow visualisation and pressure measurements from integrated pressure sensors inside the microchannel, in order to produce two-dimensional (2D) high spatial and temporal resolution two-phase heat transfer coefficient (HTC) maps across the full domain of a polydimethylsiloxane (PDMS) high aspect ratio ( $a = 22$ ) microchannel ( $D_h = 192 \mu\text{m}$ ). High spatial and temporal resolution two-dimensional wall temperature measurements and pressure data were obtained for a range of mass fluxes ( $G = 7.37\text{-}298 \text{ kg m}^{-2} \text{ s}^{-1}$ ) and heat fluxes ( $q = 13.64 \text{ to } 179.2 \text{ kW m}^{-2}$ ) using FC-72 as the working liquid. The 2D plots of HTC provided fine details of local variations during bubble nucleation, confinement, elongated bubble, slug flow and annular flow regime. The optical images from the channel top revealed the local flow regimes and were correlated with simultaneous thermal images obtained from the channel base. The 3D plots of the 2D two-phase heat transfer coefficient with time across the microchannel domain were correlated with vapour-liquid dynamics and liquid film thinning (from the contrast of the optical images) which caused suspected dryout. The correlation between the synchronised at the same frame rate high-resolution thermal and optical images will assist in a better understanding of the heat transfer mechanisms during two-phase flow boiling in microchannels. This work intends to give a better insight into heat transfer coefficient spatial variation during flow instabilities with two-dimensional heat transfer coefficient plots as a function of time during a cycle of liquid-vapour alternations.

## KEYWORDS

Two-phase heat transfer coefficients, Flow-boiling, Transparent heater, IR Thermography, Intergated Pressure sensors

## NOMENCLATURE

$a$	Aspect ratio $W_{ch}/H_{ch}$
$D_h$	Hydraulic diameter [ $\mu\text{m}$ ]
$G$	Mass flux [ $\text{kg m}^{-2} \text{s}^{-1}$ ]
$h$	Heat transfer coefficient [ $\text{W m}^{-2}\text{K}^{-1}$ ]
$H$	Height
$k$	Thermal conductivity [ $\text{W m K}$ ]
$L$	Length
$q$	Heat flux [ $\text{kW m}^{-2}$ ]
$P$	Pressure [bar]
$W$	Width
$t$	Time [s]
$x$	Axis of the channel length
$y$	Axis of the channel width

## Subscripts

ch	Channel
s1	Sensor 1 at the channel inlet
s2	Sensor 2 at the channel outlet
tp	Two-phase

## 1. INTRODUCTION

Two-phase flow boiling in microchannels is a promising technology for the cooling of microelectronic devices. However, the heat transfer mechanisms and the conditions that cause local dryout, still need to be addressed in order to be able to predict the performance of these devices. Dryout is related with flow instabilities that occur on the channel surface, which cause local overheating of the channel. As a result, the overheating causes burnout of the device.

During these flow instabilities, temperature and pressure fluctuations occur on the channel surface. Flow boiling instability is a critical issue that should be taken under consideration when designing microchannel systems. This is because during the unstable mode, temperature, pressure and mass flow rate oscillations with large amplitudes can occur on the channel surface. In recent review of Karayiannis and Mahmoud [1] the possible reasons for flow instabilities were categorized in four groups. Firstly, flow instabilities during flow boiling in microchannels can be caused by the local film evaporation during the rapid bubble axial expansion in upstream and downstream sides of the channel that induces a wall temperature jump. The second reason could be the size of the inlet / outlet manifold of the channel. It has been observed that bubbles can merge at the outlet plenum and can formate a large vapour patch which results in liquid flow blockage and high pressure drop. The third reason could be the high inlet compressibility effects induced by the confined bubble when it grows axially in both directions until it reaches the channel inlet. The fourth cause of flow instability is the nucleation at the channel inlet that can induce unstable flow mode during confined bubble axial expansion.

Although there is still conflict about the main flow boiling heat transfer mechanism in microchannels [1], thin liquid film evaporation is considered the main flow boiling heat transfer mechanism by many researchers [2-5]. Jinliang *et al.* [2] investigated the heat transfer flow boiling mechanisms in 10 silicon parallel triangular cross section microchannels of 155.6  $\mu\text{m}$  hydraulic diameter using infrared thermography technique from the base combined with high-speed microscopy from the top. A thin platinum (Pt) film was deposited at the back of the silicon chip. They used acetone as the working fluid, which has the same boiling point with FC-72 (56 °C at P = 1 atm). They found that the four characteristic flow patterns where periodically repeated in a timescale of milliseconds. The cycles of fluctuations were divided in the liquid refilling stage, bubble nucleation, growth and coalescence stage and transient annular flow stage. They observed that paired or triplet bubbles nucleated simultaneously in or very close to the channel corner at the same cross section. Then a single liquid plug appeared after the bubble nucleation, which was later separated in two parts that were pushed out of the flow field. During the transient annular flow stage the liquid at the channel corners was observed to decrease in time and after partial or full dryout occurred the liquid refilling stage was initiated. During these periodic fluctuations it was found that the pressure and temperature of the fluid was stable while the chip

presented spatial variation of the wall temperature. The temperature variation occurred due to liquid-vapour alternations at the majority of the heating area. For example, for an inlet liquid temperature of 30.8 °C, at  $G = 110.1 \text{ kg m}^{-2}\text{s}^{-1}$  and  $q = 141.92 \text{ kW m}^{-2}$  the time averaged pressure drop was 30.41 kPa and the wall temperature spatially varied from 62 to 74 °C. The heat coefficient was found to increase from 1,000 to 25,000  $\text{W m}^{-2} \text{K}^{-1}$  after a small distance from the inlet. The lowest temperatures were measured across the inlet and the outlet margins of the channel. According to the authors, the non-uniformity of wall temperature along the chip occurred due to uneven liquid distribution during the refilling stage. The camera resolution was  $320 \times 240$  pixels for the focus heating area of  $16.0 \times 4.2 \text{ mm}^2$ . Although there was simultaneous optical and thermal visualisations the optical images were not clear enough and the resolution of the IR images was poor. In addition, there was no correlation of the optical images with the heat transfer coefficients. The heat transfer coefficients were studied and compared with the classical Chens's [3] correlation and other correlations [4-10] for macro- and miniature capillary tubes by the work of Gan *et al.* [4]. They calculated the heat transfer coefficients for the experiments of the study of Xu *et al.* [4]. They found that the heat transfer coefficients in silicon microchannels are significantly decreased compared to miniature evaporators of copper or stainless steel. Therefore, they came into the conclusion that boiling heat transfer mechanism depends strongly on the surface characteristics. The macroscale correlations that were used to compare with the experimental results were found to overpredict the heat transfer. They explained that the deviation of the heat transfer coefficients calculated from available correlations resulted from the different working fluids, operating parameters compared to those used in their experiments with the silicon microchannels. They suggested that the major reason for the discrepancies comes from the differences on the surface characteristic of the smooth silicon substrate. Boiling heat transfer coefficients along the centerline of the silicon channel device were determined from Xu and Gan [11] by infrared images. The heat transfer coefficients were found to depend on the mass fluxes and the vapour mass qualities for the mass fluxes from 96 to 360  $\text{kg m}^{-2}\text{s}^{-1}$  and heat fluxes from 140 to 430  $\text{kW m}^{-2}$ , using acetone as the working liquid. They resulted that nucleate boiling mechanism is dominant because the periodic cycle of fluctuations were related to bubble nucleation, growth and departure followed by liquid refilling. The silicon microchannel chip temperatures were slightly higher at the inlet because of liquid,

then they increased with channel length and decreased again near the outlet. Other studies on flow boiling with infrared thermography were also found in the literature [12-14] but they used lower frequency rates and spatial resolution compared to this work. They also did not measure the heat transfer coefficients and did not correlate it with flow visualisations.

The two-phase heat transfer coefficients are affected by the local flow patterns [1], therefore simultaneous optical and thermal images are required in order to explain the local heat transfer changes and provide a better insight into the causes of dryout.

For the investigation of flow boiling instabilities during the unstable flow mode it is important to use pressure sensors that can be integrated in the channel in order to acquire the pressure changes. Pressure oscillations were measured in the millisecond time scale therefore high response time pressure sensors are required [15].

Although there is extensive literature [2] on the parameters that affect flow boiling heat transfer in microchannels there is still need for more spatially and temporally resolved temperature data across the full domain of the microchannel in order to obtain a better insight into flow boiling mechanisms.

For this study, infrared (IR) thermography (non-intrusive) was combined with flow visualisation in order to investigate the complex physical phenomena of two-phase flow boiling in microchannels (bubble confinement, rewetting and dryout). 2D maps of the two-phase heat transfer coefficients were produced from high spatial (15.33  $\mu\text{m}$ ) and temporal (0.015 s) resolution wall temperature measurements, obtained from the transparent indium tin oxide (ITO)/glass base, together with simultaneous pressure data from integrated pressure sensors assuming linear profile from the inlet to the outlet of the microchannel. A range of mass fluxes ( $G = 7.37\text{-}195.43 \text{ kg m}^{-2} \text{ s}^{-1}$ ) and heat fluxes ( $q = 13.64 \text{ to } 185 \text{ kW m}^{-2}$ ) were tested in order to correlate the different heat transfer trends with the flow regimes obtained from the optical images. The main contribution of this work is the highly resolved spatial and temporal temperature mapping, combined with high speed flow visualisation for a better understanding of the two-phase flow and correlate this to heat transfer.

## **2. EXPERIMENTAL METHOD**

Boiling experiments were performed using the flow loop system presented in Figure 1 (a). A magnetically coupled gear micropump was used to circulate degassed

fluorinert FC-72 ( $T_{sat} = 56\text{ }^{\circ}\text{C}$  at  $P = 1\text{ atm}$ ) at a constant flow rate through a microchannel. The liquid temperature prior to entry to the channel via the inlet was maintained at  $21 \pm 1\text{ }^{\circ}\text{C}$ . A range of mass fluxes ( $G = 7.37\text{--}298\text{ kg m}^{-2}\text{ s}^{-1}$ ) and heat fluxes ( $q = 13.64\text{ to }179.2\text{ kW m}^{-2}$ ) were tested using the microchannel presented in Figure 1b.

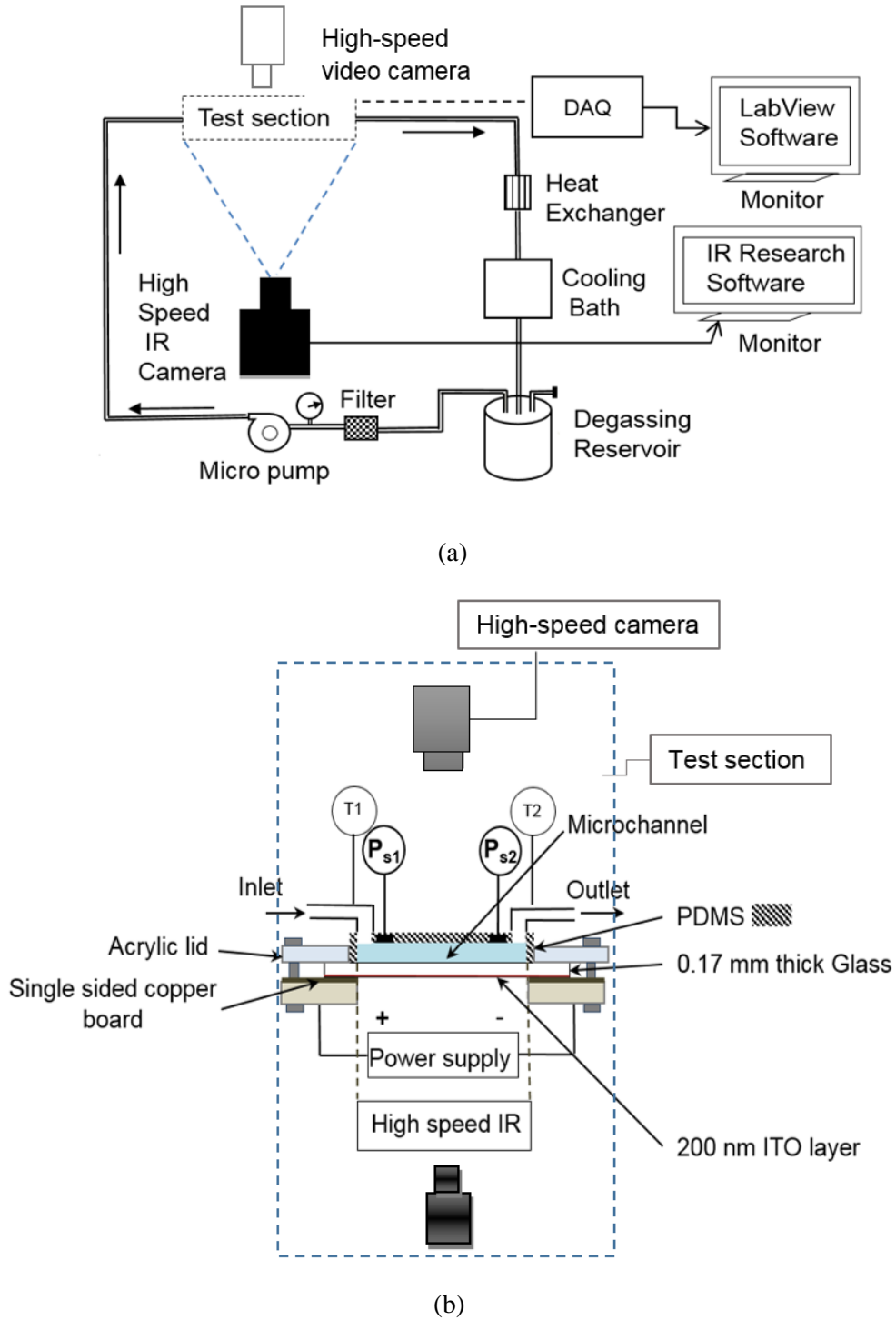


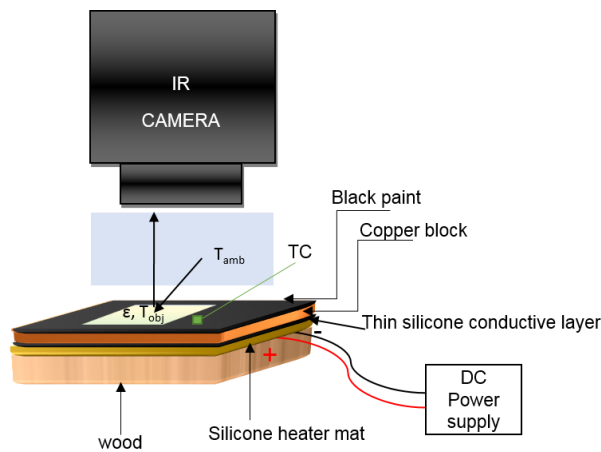
Figure 1. Schematic drawing of (a) the experimental setup, (b) the test section, which

consists of a microchannel with integrated pressure sensors ( $P_{s1}$ ,  $P_{s2}$ ).

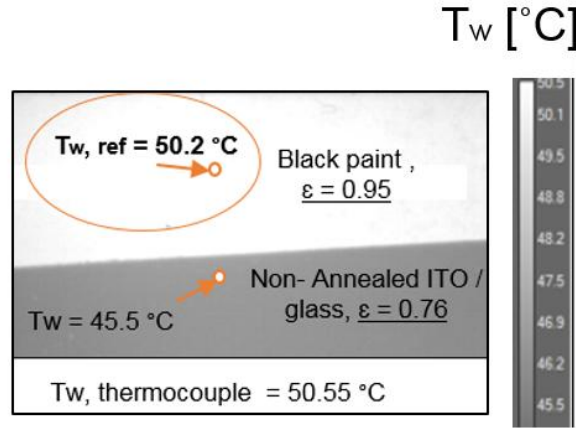
A high aspect-ratio ( $a = 22$ ) rectangular cross-section (width ( $W_{ch}$ ) = 2.26 mm, height ( $H_{ch}$ ) = 100  $\mu\text{m}$  and length ( $L_{ch}$ ) = 20 mm) polydimethylsiloxane (PDMS) microchannel, with a hydraulic diameter ( $D_h$ ) of 192  $\mu\text{m}$ , formed the test section. The PDMS microchannel was attached to the front-side of a glass microscope slide following oxygen plasma activation [16]. The backside of the 0.17 mm thick microscope glass slide ( $22 \times 50 \text{ mm}^2$ ) was coated with a 200 nm conductive, transparent thin film of indium tin oxide (ITO), to facilitate the heating of fluid in the channel. The effective area of the ITO / glass was  $2.26 \times 20 \text{ mm}^2$ . A specially designed support was used to hold the device and to provide the electrical contacts to the ITO heater. The liquid in the test section channel was heated by passing a DC current through the ITO film via two copper contacts/tracks. During heating of the liquid in the channel, a spatial map of the wall-temperature was recorded from the glass side of the device using a FLIR X6580sc high-speed infrared camera (thermal sensitivity of 20 mK) at a high resolution of  $640 \times 512$  pixel ( representing 15.39  $\mu\text{m}$  / pixel ) and a high frame rate of 200 Hz. The spectral range of the camera was 1.5 to 5.1  $\mu\text{m}$  and the detector pixel pitch was 15  $\mu\text{m}$ . A Keyence VW-600C high speed camera, mounted on a VW-9000 microscope was used to record simultaneously (at the same frame rate of IR camera) the flow in the channel.

Figure 2 (a) presents the calibration setup used for the emissivity measurements of the ITO coated glass. The calibration method followed the method used in the study of Madding [17] where they used a camera with the same wavelength range (3-5  $\mu\text{m}$ ) as in these experiments. The copper block is then attached on a silicon heater mat (8 mm  $\times$  4 mm) via a very thin electrically conductive silicone sheet (8 mm  $\times$  4 mm  $\times$  1.6 mm). The silicon heater mat is then attached on a wooden block (8 mm  $\times$  4 mm  $\times$  2 mm). The conductive thin layer of the silicone sheet ensures a good electrical contact. The sample was attached on the surface with the black paint using a thermal adhesive tape. Then, the IR camera lens was adjusted at  $30 \pm 1$  cm from the surface of the black paint. The silicon heater map was connected with a DC power supply from where the power to the heater was adjusted. The power was increased while temperature measurements were obtained by the IR camera. A K-type thermocouple was placed on the sample in order to validate the temperature measurements obtained from the IR camera. The maximum difference between the

thermocouple and the measurement from the IR camera was  $0.25\text{ }^{\circ}\text{C}$ . Figure 2 (b) shows an example of emissivity measurements for a constant power. The thermal image shows the initial temperature at one location before calibration and the emissivity measurement after the calibration by taking as reference the temperature of the black paint which has a known emissivity. The temperature of the black paint was  $50.2\text{ }^{\circ}\text{C}$  ( $\epsilon = 0.95$ ), used as a reference in order to calibrate the surface emissivity of the tested samples of ITO /glass. The ITO /glass slide is placed on the black paint and taped down and its temperature is measured to be  $38^{\circ}\text{C}$ . The temperature values are lower than the temperature from the black paint. This occurs because the radiation received by the IR camera is less than the one from the blackbody at the same temperature and so the surface will appear colder than it is unless the thermometer reading is adjusted to take into account the material surface emissivity. The same process was repeated at higher power in order to examine the change of the substrate surface emissivity with surface temperature. The surface emissivity for ITO /glass was averaged over five measurements obtained at different power and was found to be  $0.76$ . The IR research software was used in order to adjust the emissivity of the tested samples.



(a)



(b)

Figure 2. (a) Setup for calibration of surface emissivity (b) thermal image from the IR camera comparing the emissivity of ITO coated glass with black paint emissivity using a greyscale.

The two-phase heat transfer coefficients were calculated using wall temperature measurements and fluid saturation temperatures obtained from interpolating inlet and outlet pressure measurements, the latter from integrated silicon ceramic-based pressure sensors located near the inlet and outlet of the microchannel.

### 3. DATA REDUCTION

The temperature measurements were obtained from the channel outer wall of the glass base. The analysis of IR data in single-phase flow showed uniform heating of the microchannel as the temperature gradient was constant, without local temporal variations of temperature in excess of 0.2 °C. The transverse temperature profile showed a slight dip in temperature (~1°C) at the channel centre. The conversion factor for the IR images was 15.39 μm / pixel and was calibrated to the width of the microchannel.

The *Biot* number that indicates the temperature uniformity within the channel by comparing the conduction resistance to the convection resistance was calculated as:

$$Bi = \frac{h_{conv}\tau_w}{k} \quad (1)$$

where  $\tau_w$  is the channel wall thickness,  $k$  the thermal conductivity of the glass and  $h_{conv}$  is the convective heat transfer coefficient calculated from Newton's cooling law:

$$Q_{eff} = h_{conv}A(T_w - T_f) \quad (2)$$

where  $T_w$  is the outer wall temperature of the channel and  $T_f$  is the fluid temperature,  $A$  is the outer channel surface and  $Q_{eff}$  is the power transferred to the liquid during single-phase flow (eq.4). Since  $Bi \ll 1$  the difference between the inner and outer wall temperature could be neglected. The value of  $h_{conv}$  was found to vary from 1080 to 15,000  $W m^{-2} K^{-1}$  with 11.4 % uncertainty. The local microchannel pressure was interpolated assuming a linear profile of pressure from inlet to outlet, following previous studies.

The heat transfer losses for single phase flow conditions were estimated from the energy balance:

$$Q_{loss} = Q_{ITO} - Q_{eff} \quad (3)$$

where  $Q_{ITO}$  is the total input power provided to the ITO glass surface ( $22 \times 50 \text{ mm}^2$ ), determined using Joule's first law and  $Q_{eff}$  is the effective heat transferred to the liquid during single-phase flow which was estimated from:

$$Q_{eff} = \dot{m}c_{p,l}(T_{l,out}-T_{l,in}) \quad (4)$$

where  $T_{l,in}$  and  $T_{l,out}$  are the inlet and outlet liquid temperatures,  $\dot{m}$ , the liquid mass flow rate ( $kg s^{-1}$ ) and  $c_{p,l}$ , the liquid specific heat capacity, calculated at the mean temperature of the liquid. The maximum heat transfer losses for single-phase were calculated to be 5.5 %.

For two-phase flow conditions, the heat transfer losses from the channel surface to the surroundings were evaluated from:

$$Q_{loss}(x, y) = Q_{conv}(x, y) + Q_{rad}(x, y) \quad (5)$$

considering both convection ( $Q_{conv}$ ) and radiation ( $Q_{rad}$ ) losses. Then  $Q_{eff}$  which is the power transferred to the fluid from the channel, was estimated from equation (3) with known  $Q_{loss}$ .

The width of the microchannels was aligned with the  $y$  axis and the channel length with the  $x$  axis.

The convective losses were estimated from:

$$Q_{conv}(x, y) = h_{conv} A(T_{w,IR}(x, y) - T_{amb}) \quad (6)$$

where  $h_{conv}$  is the convective heat transfer coefficient of air estimated from empirical correlations for natural convection [18] and  $A$ , the microchannel heated surface area,  $T_{w,IR}(x, y)$ , the temperature distribution of the microchannel surface obtained using the IR camera and  $T_{amb}$  the ambient temperature close to the surface.

The radiative losses were estimated from :

$$Q_{rad}(x, y) = \varepsilon \omega A (T_{w,IR}^4(x, y) - T_{amb}^4) \quad (7)$$

where  $\varepsilon$ , the surface emissivity of the microchannel and  $\omega = 5.67 \times 10^{-8} \text{ Wm}^{-2}\text{K}^{-4}$ , the Stefan–Boltzmann constant. The values obtained for  $Q_{conv}$  (uncertainty of 2.35 %) ranged between 0.003 W to 0.005 W and the values for  $Q_{rad}$  ranged between  $2.15 \times 10^{-7}$  to 0.00047 W (uncertainty of 0.15 %).

The average heat flux at the wall was calculated from:

$$q(x, y) = \frac{Q_{eff}}{A} \quad (8)$$

The local liquid temperature was calculated based on the assumption that all the effective heat flux was used to heat up the liquid:

$$T_l(x, y) = \frac{(q(x, y) \cdot P_h \cdot z)}{c_{p,l} \cdot \dot{m}} + T_{l,in} \quad (9)$$

where  $P_h$  is the channel heated perimeter,  $z$ , the distance from the channel inlet,  $T_{l,in}$  is the inlet temperature of the liquid and  $T_{sat}(x)$ , the local saturation temperature calculated from local pressure along the microchannel. The value of  $T_{sat}$  is dependent on local pressure and this dependence was implemented in the calculations of the heat transfer coefficient for precision (many previous studies have used a fixed value for  $T_{sat}$  ignoring the pressure drop in the microchannel).

The local heat transfer coefficient for single-phase flow was calculated using:

$$h_{sp}(x, y) = \frac{q(x, y)}{(T_{w,IR}(x, y) - T_l(x, y))} \quad (10)$$

The local two-phase heat transfer coefficient for subcooled ( $x_e < 0$ ) flow was determined as:

$$h_{tp}(x, y) = \frac{q(x, y)}{(T_{w,IR}(x, y) - T_l(x, y))} \quad (11)$$

where  $x_e$  is the vapour quality.

The local two-phase heat transfer coefficient for saturated ( $x_e > 0$ ) flow was determined as:

$$h_{tp}(x, y) = \frac{q(x, y)}{(T_{w,IR}(x, y) - T_{sat}(x, y))} \quad (12)$$

For the experiments presented in this paper, the main uncertainties are identified in Table 1.

**Table 1.** Summary of measurements uncertainties.

Parameter	Maximum Uncertainty
Standard K-type thermocouple	$\pm 0.5$ °C
Pressure sensors	0.20 %
DC power supply	$\pm 1$ % of reading
IR camera measured temperature	$\pm 1$ °C (from 20 °C to 120 °C)
Pump volumetric velocity	0.5 %
Mass flux	9%
Heat flux	6 %
Heat transfer coefficient	11%
Vapour quality	3.2 %

#### 4. RESULTS AND DISCUSSION

This section presents local two-phase heat transfer data correlated with simultaneous flow visualizations, as well as bubble dynamics and pressure drop. The local spatio-

temporal evolution of the heat transfer coefficient was examined for imposed mass fluxes ( $G = 7.37\text{-}298 \text{ kg m}^{-2} \text{ s}^{-1}$ ) and heat fluxes ( $q = 13.64 \text{ to } 179.2 \text{ kW m}^{-2}$ ).

#### 4.1 Local wall temperature measurements

The temperature data were obtained using the IR camera from the ITO/ glass channel base. Figure 3 shows wall temperature measurements which were obtained from an IR video recording of 60 s at three positions (1a,1b,1c) across the channel entrance ( $x_I = 0 \text{ mm}$ ) width for  $G = 14.78 \text{ kg m}^{-2} \text{ s}^{-1}$  and  $q = 43.80 \text{ kW m}^{-2}$ .  $T_{w, aI}$  was obtained at the left channel edge (a),  $T_{w, bI}$  at the centre (b) of the channel and  $T_{w, cI}$  at the right channel edge (c). Figure 3a shows the schematic of the channel and the positions of the measurements across the channel width. Figure 3b shows the local temperature measurements as a function of time. Periodic fluctuations of wall temperature result from confined bubble growth in the channel.

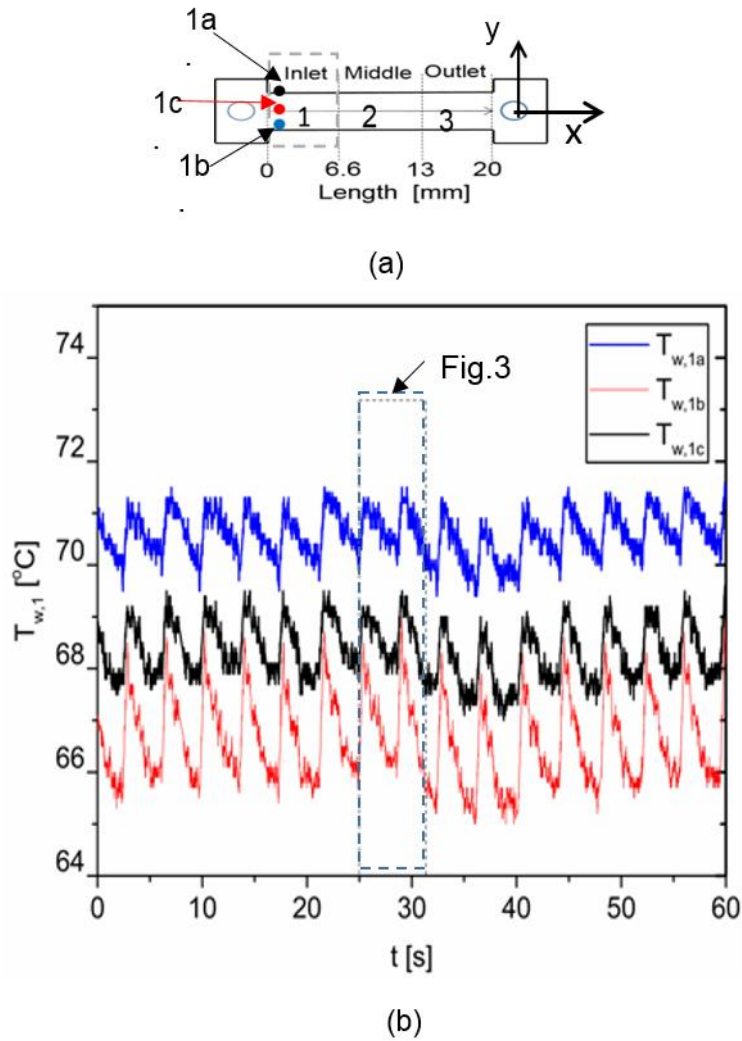


Figure 3. (a) Position (1a,1b,1c) of wall temperature measurements at the channel entrance (b) local wall temperature measurements, obtained at the channel entrance as a function of time during two-phase flow boiling for  $G = 14.78 \text{ kg m}^{-2}\text{s}^{-1}$  and  $q = 43.80 \text{ kW m}^{-2}$ . The measurements were obtained at three locations across the channel width ( $T_{w, a1}$ : left channel edge,  $T_{w, b1}$ : centre,  $T_{w, c1}$ : other channel edge) at the channel entrance (position 1).

Non uniform wall temperature was obtained across the channel entrance width. For example, when the temperature value of  $71.3 \text{ }^\circ\text{C}$  was measured at one edge (1a) of the channel,  $69.2 \text{ }^\circ\text{C}$  was the temperature obtained simultaneously across the opposite edge (1c) and  $68.4 \text{ }^\circ\text{C}$  at the channel centre (1b). Therefore, a maximum temperature difference of  $2.9 \text{ }^\circ\text{C}$  was measured to occur from the centre to the edges. The periodic temperature fluctuations were characterised as low amplitude high frequency fluctuations and high amplitude low frequency fluctuations and were related to bubble confinement effects. The flow patterns observed from the optical images. These types of temperature fluctuations were also referred by previous studies [2,5]. The high spatial and temporal resolution temperature data were used for the calculation of the

2D local heat transfer coefficients.

## 4.2 Local two phase heat transfer coefficients ( $h_{tp}$ )

### 4.2.1 Local two phase heat transfer coefficients ( $h_{tp}$ ) at $q < 45 \text{ kW m}^{-2}$

High heat transfer coefficients ( $1,100\text{-}16,000 \text{ W m}^{-2} \text{ K}^{-1}$ ) were obtained at low mass fluxes ( $7.37\text{-}14.78 \text{ kg m}^{-2}\text{s}^{-1}$ ). From the simultaneous flow visualisations, bubble nucleation, growth and confinement and annular flow regimes were the flow patterns observed to occur periodically along the channel. Figure 4 shows the local heat transfer coefficients as a function of time for the channel entrance (position 1). The local two-phase heat transfer coefficients in time were correlated with optical images (Figure 5) from  $t = 25 \text{ s}$  to  $31 \text{ s}$ , in order to relate the observed flow patterns with the periodic temperature fluctuations (Figure 3).

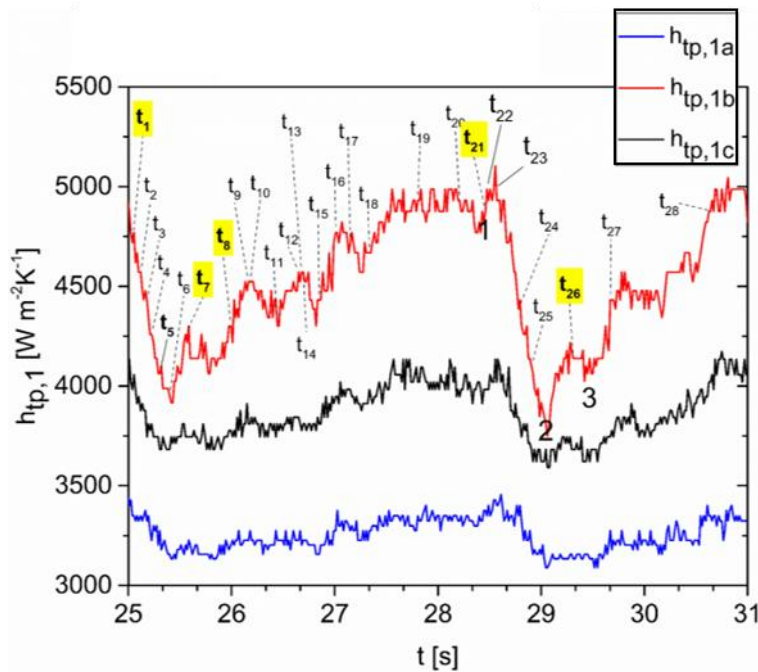


Figure 4. Local two-phase heat transfer coefficients across 3 positions of the channel entrance. The positions 1a, 1b, 1c are shown in schematic of Figure 2 (a). The locations where  $h_{tp, 1a}$ ,  $h_{tp, 1b}$  and  $h_{tp, 1c}$  were calculated are presented in the schematic on the right top of the graph.

The  $h_{tp}$  in Figure 4 were produced from the wall temperature temporal profiles shown in Figure 3 (b). Figure 5 shows the simultaneous flow patterns obtained along the microchannel from 0 to 10 mm (from channel entrance).

Figure 5 shows the main flow patterns observed during flow boiling for  $G = 14.78 \text{ kg m}^{-2}\text{s}^{-1}$  and  $q = 43.80 \text{ kW m}^{-2}$ . Bubbly, slug and annular flow were the main flow

patterns. The elongated bubble was formed from a single isolated bubble and not as a result of bubble coalescence. From the flow visualizations in Figure 5, bubble nucleation was observed to occur adjacent to the superheated edge (1c) of the channel entrance ( $t_{29}$ ). Bubble nucleation was also observed to occur simultaneously at the other upper channel edge (side of 1a) but close to the outlet. Therefore, two nucleation sites were observed to cause bubble nucleation under certain conditions along the whole channel length.

The correlation between Figure 3 and Figure 5 revealed that the low amplitude temperature fluctuations started when bubble nucleation occurred at the channel entrance, adjacent to the superheated channel sidewall ( $t_{10} = 26.180$  s).

The spherical bubble started growing symmetrically while moving adjacent to the wall. When the spherical bubble departed from the wall and moved to the centre of the channel, it started growing faster ( $t_{11} = 26.445$  s). Then, the bubble was confined by the channel height and as a result it started growing in widthwise direction. At  $t_{12} = 26.652$  s the bubble occupied the whole channel width ( $t_{12} = 26.652$  s) and axial growth of the bubble nose (end of bubble moving streamwise) occurred. At  $t_{14} = 26.691$  s, a bullet-shape bubble was formed. A bullet-shape bubble was formed when the front of the bubble started growing axially while the bubble fully occupied the channel cross section at a position close to the curved end of the bubble (tail) which was emphasized with a red arrow, in parallel to the width of the channel ( $t_{13} = 26.673$  s). At  $t_{15} = 26.869$  s, the elongated bubble was flushed out from the channel because of the incoming liquid flow. This flow instability was accompanied by a low amplitude temperature fluctuation, which resulted in the decrease of the local heat transfer coefficient in time. The two-phase heat transfer coefficient dropped by a maximum value of  $250 \text{ W m}^{-2} \text{ K}^{-1}$  (Figure 6). The correlation between the heat transfer coefficient fluctuations that are shown in Figure 3 and the flow visualisation images of Figure 5 showed that the high amplitude temperature fluctuations started after the bubble was observed to fully occupy the width of the channel entrance ( $t_{22} = 28.555$  s). After the bubble occupied the channel width, it started growing axially forming an elongated bubble. Abrupt axial expansion of the bubble occurred as a result of the high aspect ratio of the microchannel. This resulted in flow reversal. The confined bubble at the channel inlet was found to enhance locally the heat transfer coefficient ( $t_{22}$ - $t_{23}$ , Figure 5). The elongated bubble axial growth along the whole channel length, resulted in the establishment of annular flow regime ( $t_{25} = 28.891$  s) along the whole

channel domain. The vapour was then flushed out by the incoming liquid flow and a new cycle of low amplitude temperature fluctuation started when the bubble nucleated at the channel entrance ( $t_8 = 25.995$  s). The flow instability during axial expansion of the bubble at the channel entrance was accompanied by flow reversal and a high amplitude temperature fluctuation occurred which resulted in local decrease of the local heat transfer coefficient by a maximum of  $1250 \text{ W m}^{-2} \text{ K}^{-1}$  (Figure 4).

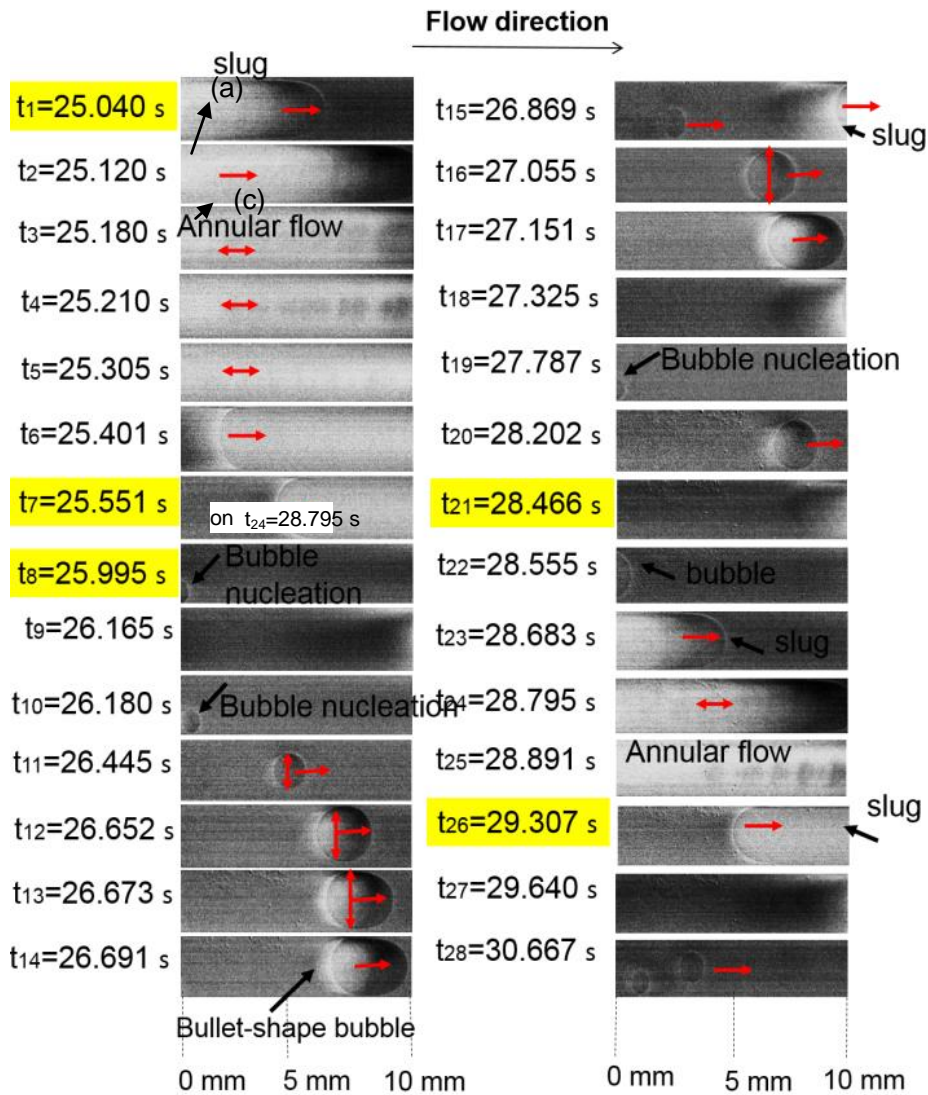
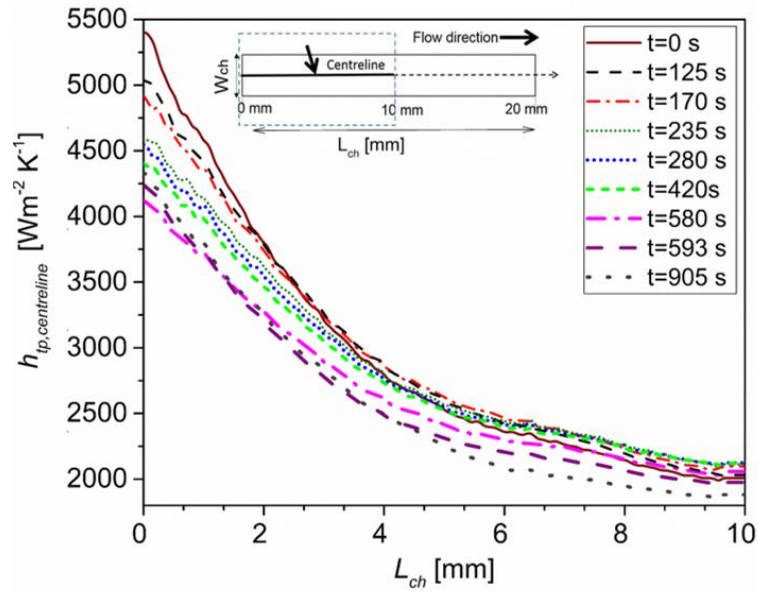
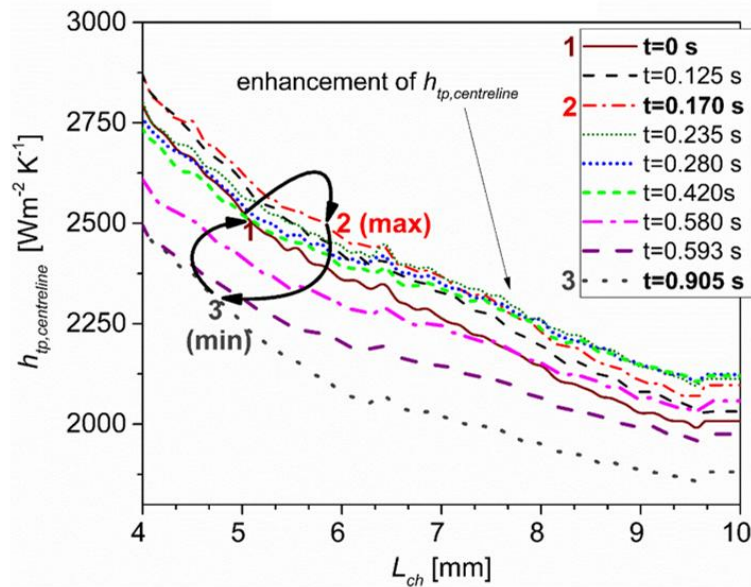


Figure 5. Flow patterns observed with simultaneous thermal images from the channel base during flow boiling in the channel from 0 to 10 mm. The optical images were correlated with the heat transfer coefficients at the channel entrance, presented in Figure 4.

The high amplitude fluctuations were further analyzed by correlating the local heat transfer coefficient profiles which were obtained along the channel centreline (Figure 6) with the thermal patterns from the IR thermal images (Figure 7).



(a)



(b)

Figure 6. (a) Local two-phase heat transfer coefficient profiles as a function of time along the channel centerline (from 0 to 10 mm) for  $G = 14.78 \text{ kg m}^{-2}\text{s}^{-1}$  and  $q = 43.80 \text{ kW m}^{-2}$ . (b) Heat transfer coefficient as a function of length from 4 to 10 mm. The cycle of the high amplitude fluctuation is represented with arrows and is related to Figure 7.

Figure 6 (a) presents the local two-phase heat transfer coefficient profiles as a function of time along the channel centreline (from 0 to 10 mm) for  $G = 14.78 \text{ kg m}^{-2}\text{s}^{-1}$  and  $q = 43.80 \text{ kW m}^{-2}$ . The high amplitude heat transfer coefficient fluctuation cycle was depicted in Figure 6 (b) using arrows and numbers from 1 to 3 that show

the sequence of events. The local heat transfer coefficients presented in Figure 6 were obtained from the thermal images shown in Figure 7. The shape of the bubbles was obtained from the simultaneous optical images presented in previous Figure 5.

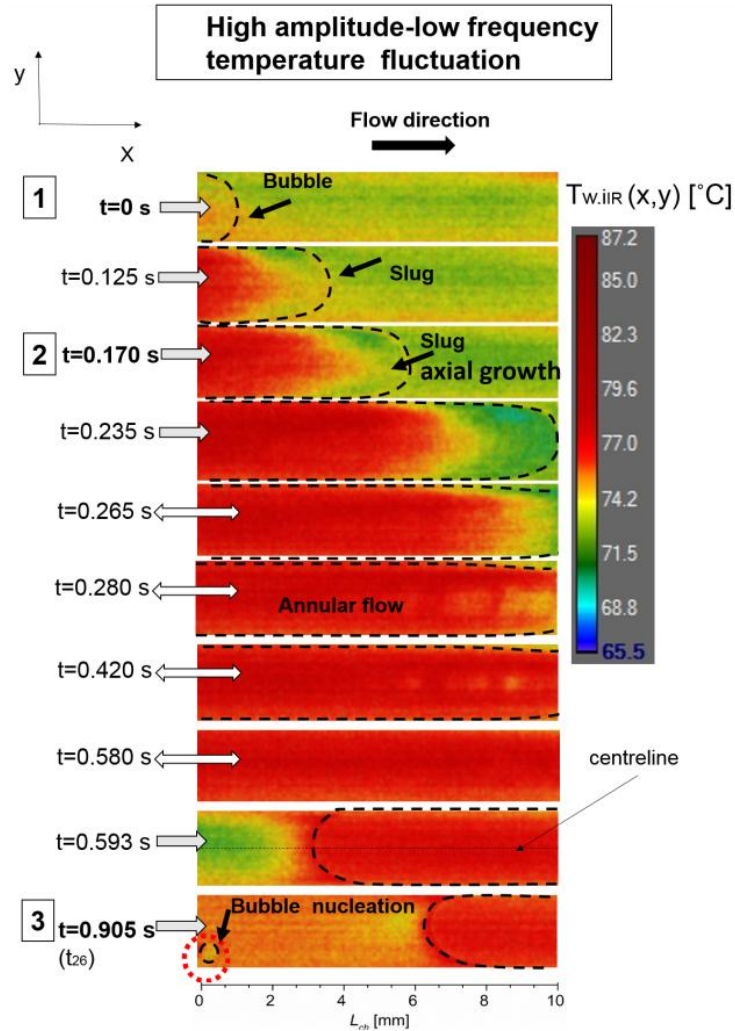


Figure 7. Thermal images obtained for  $G = 14.78 \text{ kg m}^{-2}\text{s}^{-1}$  and  $q = 43.80 \text{ kW m}^{-2}$  from 0 to 10 mm. The numbers 1, 2, 3 were related with the fluctuation cycle shown in Figure 6 (b).

From Figure 6 (b) and Figure 7 was observed that the axial growth of the elongated bubble at  $t = 0.170 \text{ s}$  resulted in the local increase of the local heat transfer coefficient up to  $125 \text{ W m}^{-2} \text{ K}^{-1}$  (from 4.2 to 6.8 mm) along the channel centerline. However, after the further axial elongation of the confined bubble along the channel, the bubble occupied the channel cross section and channel length and resulted in annular flow regime. During this regime the two-phase heat transfer coefficient decreased because of suspected local dryout at the channeledges. Liquid film thinning at the channel edges during annular flow regime was also observed by Jinliang *et al.* [2]

using infrared thermography combined with high speed microscopy for triangular cross section silicon microchannels. At  $t = 0.580$  s the heat transfer coefficient was observed to decrease along the centerline, possibly due to evaporation of the liquid film at the channel centre.

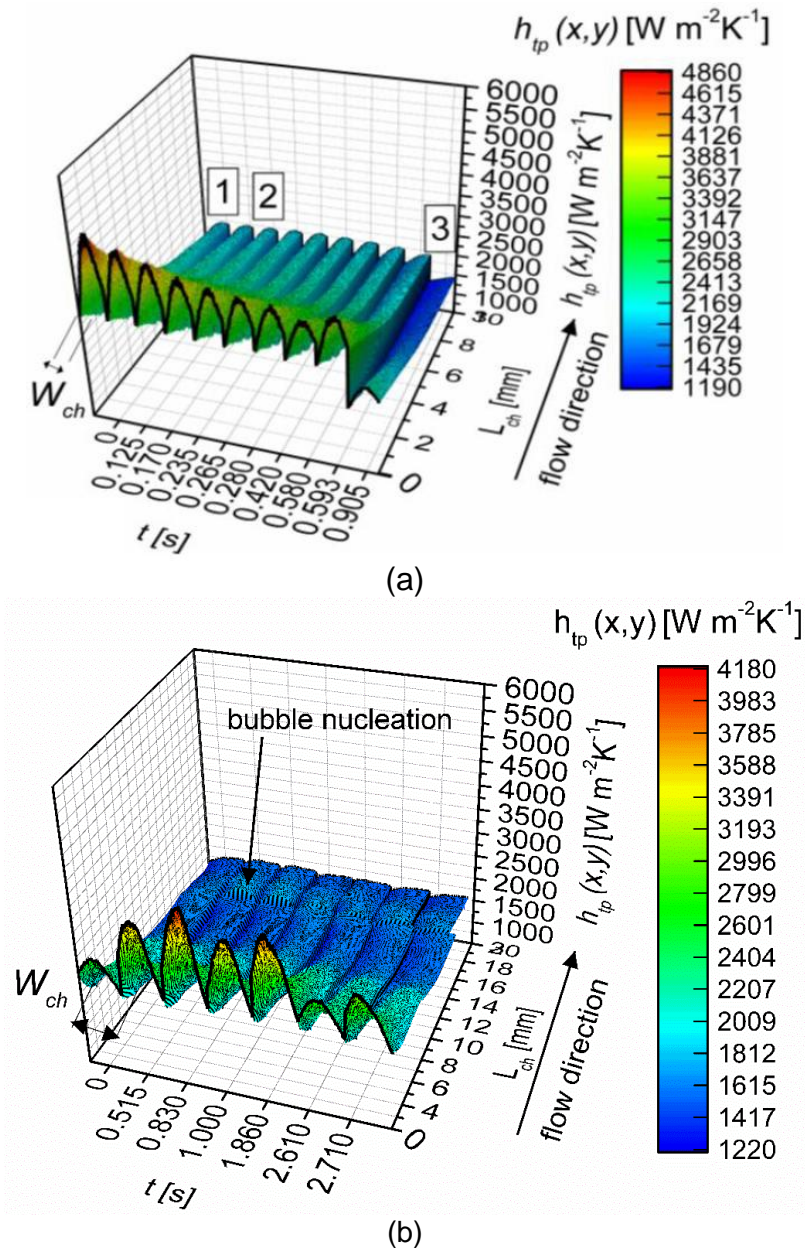


Figure 8. (a) 3D plot of the two-dimensional two-phase heat transfer coefficient distribution,  $h_{tp}(x,y)$  across microchannel for  $G = 14.78 \text{ kg m}^{-2}\text{s}^{-1}$  and  $q = 43.80 \text{ kW m}^{-2}$  from 0 to 10 mm of the channel length. The numbers 1, 2, 3, are related to the IR images shown in Figure 7 and refer to bubble confinement, bubble axial expansion and (b) 3D plot of the two-dimensional two-phase heat transfer coefficient distribution of  $h_{tp}(x,y)$  across the whole microchannel length for  $G = 14.78 \text{ kg m}^{-2}\text{s}^{-1}$  and  $q = 47.78 \text{ kW m}^{-2}$ .

Figure 8a shows the 3D plot of the two-dimensional  $h_{tp}(x,y)$  spatial variations

during confined bubble axial expansion for  $G = 14.78 \text{ kg m}^{-2}\text{s}^{-1}$  and  $q = 43.80 \text{ kW m}^{-2}$ .  $h_{tp}(x,y)$  is presented as a function of time for the length of 10 mm from the channel entrance. The results for  $h_{tp}(x,y)$  of Figure 8a were obtained using the two-dimensional wall temperature measurements from Figure 7. The heat transfer coefficient gradient was almost constant without any spatial variations along the channel length. The maximum heat transfer coefficient for all cases was measured at the centre of the channel ( $4,371 - 4,860 \text{ W m}^{-2} \text{ K}^{-1}$ ) entrance width during the axial growth of the confined bubble.  $h_{tp}(x,y)$  varied significantly ( $2,413 - 4,860 \text{ W m}^{-2}\text{K}^{-1}$ ) across the channel width, from the entrance to the position of 4.5 mm. The cross section profile from 4.5 to 10 mm, showed a smaller variation, from 1,190 to 2,413  $\text{W m}^{-2}\text{K}^{-1}$ , which was caused by liquid film thinning and suspected dryout at the channel edges.

The flow boiling two-phase heat transfer coefficients of the whole microchannel domain from 0 to 20 mm are presented in Figure 8b for the same mass flux as in Figure 8a and a higher heat flux of  $q = 47.78 \text{ kW m}^{-2}$ .  $h_{tp}(x,y)$  varied from 4,180 to 1,220  $\text{W m}^{-2}\text{K}^{-1}$  during the flow instability cycle of 2.710 s.  $h_{tp}(x,y)$  was found to increase at the entrance and at the outlet (18-20 mm) while it decreased in the middle section. This heat transfer coefficient trend was found also in the study of Jinliang *et al.* [2] but for multi-parallel silicon microchannels of triangular cross section of  $D_h = 155.4 \text{ }\mu\text{m}$ . The two-phase heat transfer coefficient reached the maximum value of 4,180  $\text{W m}^{-2}\text{K}^{-1}$  at the centre of the channel width at the entrance. This occurred at 0.830 s and 1.860 s during the flow instability cycles shown in Figure 8(b). The high heat transfer coefficient at the channel entrance was related to bubble full confinement (by the depth and width of channel) just bubble axial expansion occurrence. At the inlet section there is high possibility of liquid phase existence on the heater base which resulted in better heat transfer. The increase of the two-phase heat transfer coefficient at the very outlet was related with bubble nucleation at 18 mm (Figure 8 (b)). Bubble nucleation and confined bubble growth along the channel resulted in decrease of the local temperature at this position and increase of the heat transfer coefficient.

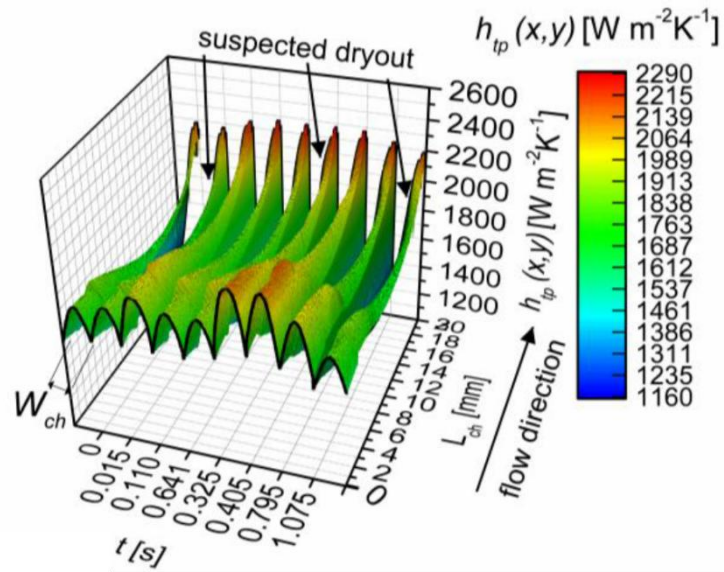
#### 4.2.2 Local two phase heat transfer coefficients ( $h_{tp}$ ) at heat fluxes $q > 45 \text{ kW m}^{-2}$

At constant mass flux, for high heat flux ( $q > 45 \text{ kW m}^{-2}$ ) deterioration of heat transfer occurred at the channel outlet as a result of the suspected intermittent dryout.

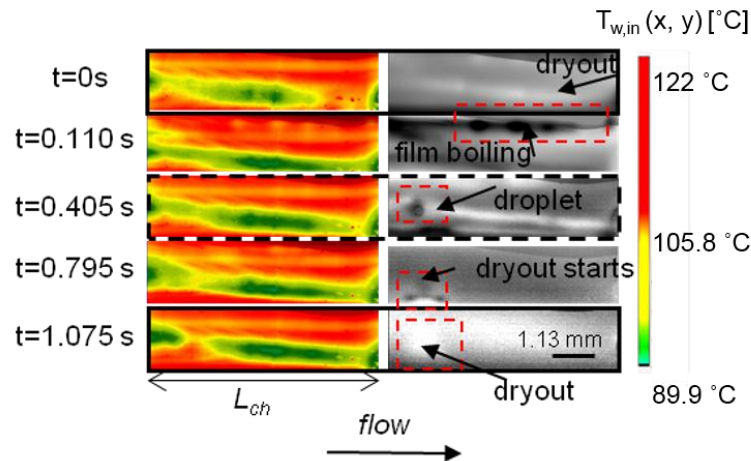
Figure 9 (a) shows the heat transfer coefficient distribution as a function of time for  $G = 14.78 \text{ kg m}^{-2}\text{s}^{-1}$  and the high heat flux of  $q = 92.3 \text{ kW m}^{-2}$ . The 3D plot revealed a considerable difference of the heat transfer coefficient distribution from the channel centre to the edges (Figure 9 (a)). The highest variation of the HTC profile

across the channel width was measured after 12 mm, and it ranged from 1,160 to 2,290 W m<sup>-2</sup> K<sup>-1</sup>. The difference in the cross sectional profile of the  $h_{tp}(x,y)$  at the outlet (from 10 to 20 mm) compared to the inlet, showed no maximum at the centre of the channel cross section. The position of maximum  $h_{tp}(x,y)$  was measured to occur at one edge of the channel and not at the centre of the channel. This could be explained due to liquid evaporation of the elongated bubble from the side attached to the channel where there is a thin liquid film. Figure 9 (a) shows that the profile of the cross sectional  $h_{tp}(x,y)$  at the outlet was found linear with channel width. In contrast, the profile of  $h_{tp}(x,y)$  at the inlet section (from 0 to 10 mm) was a curve with a maximum at the channel centre. The linearity at the outlet profile resulted from the local dryout of the liquid at the channel centre and one side of the channel at the outlet. The flow patterns which are depicted in Figure 9 (b) were observed from optical images from PDMS recorded simultaneously with the IR thermal images from the channel base.

Based on the contrast of the flow visualisations, the light (white colour) regions of the optical images were related to suspected dryout of the channel wall and were correlated with  $h_{tp}(x,y)$ . At high heat fluxes ( $q > 45$  kW m<sup>-2</sup>), the heat transfer coefficient decreased periodically during the occurrence of flow instability cycles. These cycles were characterised by bubble coalescence, transient annular / churn flow. During the appearance of annular flow regime, local suspected dryout occurred at the channel surface. In particular, some areas around the centerline of the channel appeared to be white in the optical images, which was related to suspected dryout during annular flow regime. Suspected dryout occurred only at one side of the channel outlet for a short time in milliseconds scale. The side for the occurrence of the suspected dryout at the wall was the location where bubble nucleation was suppressed. These observations were extracted from the simultaneous flow visualisations (Figure 9 (b)).



(a)



(b)

Figure 9. (a) 2D heat transfer coefficient across the full domain of the channel as a function of time for  $G = 14.78 \text{ kg m}^{-2} \text{ s}^{-1}$  and  $q = 92.3 \text{ kW m}^{-2}$ . (b) Correlation between the thermal images obtained using the IR camera and the optical images for the channel outlet from 10 to 20 mm at 200 Hz. The images were related with the 3D plots of the heat transfer coefficient (Figure 8).

Figure 9 (a) shows the non uniform distribution of the heat transfer coefficient at the channel outlet ( $L_{ch}$ : 14-20 mm). Correlation with the simultaneous images shown in Figure 9(b) reveals that directly after suspected dryout at the channel wall near the edge, rewetting of the channel walls occurred firstly at the channel edges. Rewetting at the channel edges occurred due to the capillary wicking effect. Rigorous film boiling commenced adjacent to the edges of the channel directly after rewetting. Film

boiling was considered when bubble nucleation occurred in the superheated liquid layers adjacent to the channel edges.

Figure 9 (b) shows that there is partial dewetting of the channel during the annular /churn flow regime for  $G = 14.78 \text{ kg m}^{-2}\text{s}^{-1}$  and  $q = 92.3 \text{ kW m}^{-2}$  mainly at the outlet of the channel (from 10 mm to 20 mm). This dewetting occurred due to suspected local dryout of the liquid on the channel surface. At  $t = 0.405 \text{ s}$ , dewetting occurred when the bubbles during film boiling were entrained in the vapour film resulting in the formation of liquid drops entrained in the vapour core. The high spatial resolution of the thermal images showed that the drop was evaporating while it was moving towards the channel edge, causing dewetting of the liquid below the vapour core (white spot,  $t = 1.075 \text{ s}$ ). Figure 9 (b) shows that individual superheated drops of the liquid which moved in the vapour annular. During this phenomenon, the flow loses its stability and the vapour annular diverges and converges with a high frequency.

#### **4.2.3 Heat transfer coefficient distributions at high mass flux**

Figure 10 shows results from the local two-phase heat transfer coefficient profiles calculated along the channel centerline. The two-phase heat transfer coefficients were presented as a function of the channel length from 0 to 10 mm, for  $G = 36.87 \text{ kg m}^{-2}\text{s}^{-1}$  and  $q = 119.47 \text{ kW m}^{-2}$ . The maximum  $h_{tp, \text{ centerline}}$  was measured at the channel entrance ( $x_l = 0 \text{ mm}$ ). In general,  $h_{tp, \text{ centerline}}$  decreased as a function of length from 0 to 6.2 mm. However it increased again from 6.2 mm to 8 mm and dropped again from 8 mm to 10 mm. The variation of  $h_{tp, \text{ centerline}}$  with channel length was characterised by local dips and peaks that probably depend on the liquid distribution on the channel base.

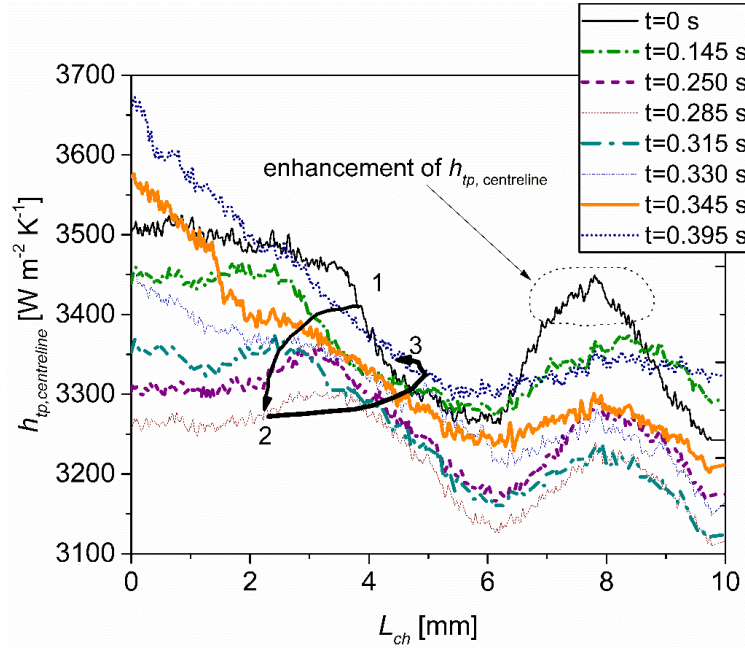
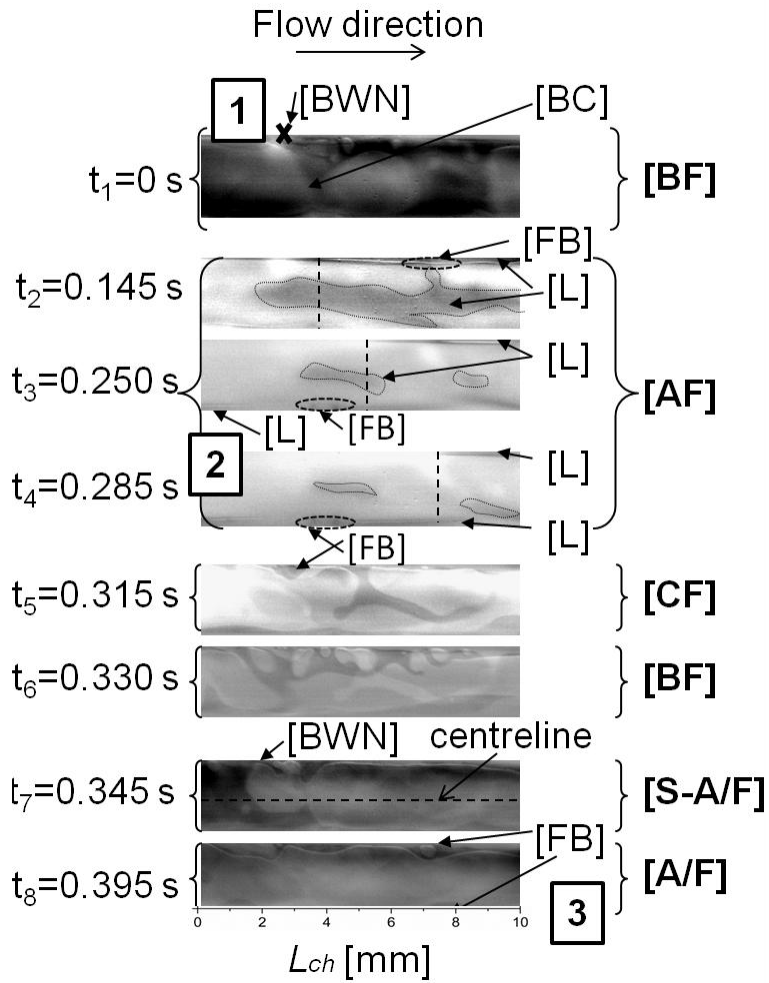


Figure 10. Local profiles of the two-phase heat transfer coefficient as a function of the channel length from 0 to 10 mm, for  $G = 36.87 \text{ kg m}^{-2}\text{s}^{-1}$  and  $q = 119.47 \text{ kW m}^{-2}$ .

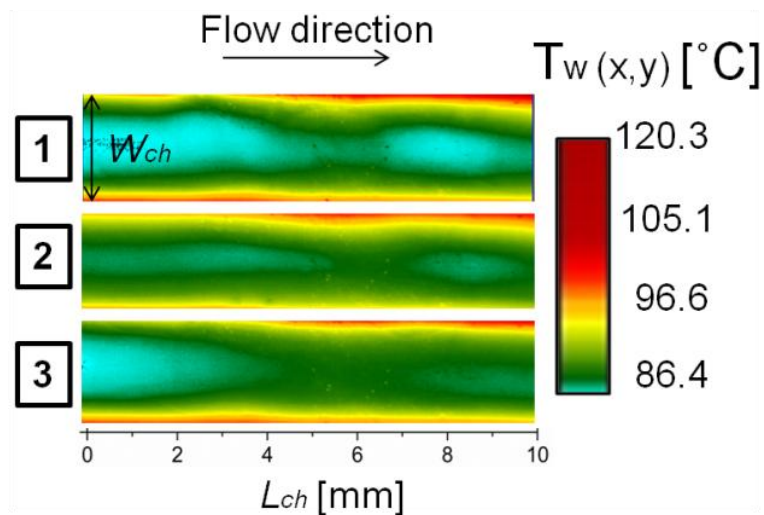
Figure 10 presents the  $h_{tp,centerline}$  at  $t = 0 \text{ s}$  was enhanced, from 6.2 mm ( $3,265 \text{ W m}^{-2} \text{ K}^{-1}$ ) to 7.84 mm. Particularly, it peaked at 7.84 mm with a maximum value of  $3,444.1 \text{ W m}^{-2} \text{ K}^{-1}$ .  $h_{tp,centerline}$  fluctuated also in time as a result of the local temperature and pressure fluctuations. The numbers 1, 2, 3 in Figure 10 show the sequence of events during one cycle offlow instability.  $h_{tp,centerline}$  for  $x_1 = 0 \text{ mm}$  (channel entrance) fluctuated between  $3,700$  to  $3,100 \text{ W m}^{-2} \text{ K}^{-1}$  during a cycle of wall temperature and pressure fluctuation, from  $t = 0 \text{ s}$  to  $t = 0.395 \text{ s}$ . At higher mass flux of  $G = 36.87 \text{ kg m}^{-2}\text{s}^{-1}$  and high heat flux of  $q = 119.47 \text{ kW m}^{-2}$  the high amplitude low frequency temperature fluctuations occurred with lower amplitude compared to lower mass fluxes of  $G = 14.78 \text{ kg m}^{-2}\text{s}^{-1}$  and  $q = 92.3 \text{ kW m}^{-2}$ . The local two-phase heat transfer coefficients were correlated with the flow patterns in Figure 12. The local two-phase heat transfer coefficient fluctuations occur as a result from bubble coalescence at the channel centre. The decrease in local heat transfer coefficient profiles occurs during the transient annular flow regime as a result of local dryout (white areas).

Figure 11 (a) shows flow patterns that were captured simultaneously with the IR thermal images presented in Figure 11 (b) for  $G = 36.87 \text{ kg m}^{-2}\text{s}^{-1}$  and  $q = 119.47 \text{ kW m}^{-2}$ . The wall temperature measurements in Figure 11 (b) revealed the wall temperature distribution at the channel base during a cycle offlow instability. The periodic cycle of flow instability was characterized with the numbers 1, 2, 3 that

show the sequence of the events. The numbers were also related to the local two-phase heat transfer coefficient profiles along the centerline shown in Figure 10. The flow direction was from the left to the right. Figure 11 (b) shows that the wall temperature ranged from 86.4 °C to 120.3 °C. The high wall temperatures between 105.1 °C and 120.3 °C were measured adjacent to the channel upper right corner (red color). These temperature values were very high and occurred as a result of the suspected dryout of the liquid film near the upper edge during the annular flow regime ( $t = 0.285$  s). The white areas on the upper right edge show the existence of suspected dryout in Figure 11 (a) for  $t = 0.285$  s. Bubble nucleation was observed to occur at the channel edges near the entrance and the outlet. The bubbles were growing adjacent to the wall. Coalescence between bubbles, resulted in the formation of large agglomerates ( $t_1 = 0$  s). Dimpled liquid areas were observed at the vapour base during the annular flow regime. The dimpled liquid areas appeared to decrease in size from  $t_2$  to  $t_4$ . The dashed lines show the location where liquid (at the right of the dashed line) exists between the vapour and the edge of the channel sidewall. At the left side of the dashed line suspected dryout of the liquid was observed to occur.



(a)



(b)

Figure 11. (a) Flow patterns captured with high speed imaging (200 Hz) from  $t = 0$  s to  $t = 0.395$  s simultaneously with the thermal images presented in Figure 11 (b) for  $G = 36.87$  kg  $m^{-2}s^{-1}$  and  $q = 119.47$  kW  $m^{-2}$ . (b) Wall temperature measurements were obtained from IR thermal images. The numbers 1, 2, 3 reveal the sequence of the thermal patterns during a cycle of the flow instability.

Table 2

Flow regimes, observed to occur during two-phase flow boiling the microchannel.

Flow regimes	Abbreviation
Bubbly Flow	[B/F]
Bubble wall nucleation	[BWN]
Single bubble flow	[S-B/F]
Bubble Coalescence	[BC]
Slug Flow	[S/F]
Bullet-shape bubble	[B-S B]
Slug-Annular Flow	[S-A /F]
Annular Flow	[A/F]
Annular Dispersed Flow	[A-D/F]
Churn Flow	[CH/F]
Film Boiling	[FB]
Suspected liquid film dryout	[S-DRY]
Drops	[DRO]

Figure 12 shows the  $h_{tp}(x,y)$  during a cycle of wall temperature and pressure fluctuations (from  $t = 0$  s to  $t = 0.395$  s). for  $G = 36.87$  kg m<sup>-2</sup>s<sup>-1</sup> and  $q = 119.47$  kW m<sup>-2</sup>.

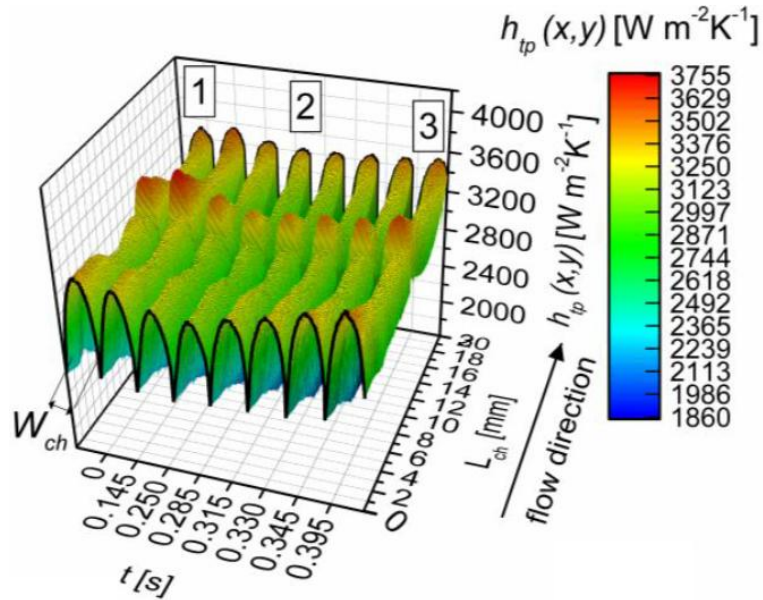


Figure 12. High spatial and temporal resolution 3D plot of two-dimensional  $h_{tp}(x,y)$  with time for the whole microchannel domain for  $G = 36.87$  kg m<sup>-2</sup>s<sup>-1</sup> and  $q = 119.47$  kW m<sup>-2</sup>.

The 3D plot in Figure 12 shows the dips and peaks of the  $h_{tp}(x,y)$  along the whole channel domain, from the entrance to the outlet. The two-dimensional two-phase

heat transfer coefficient values vary from 1,880 to 3,755 W m<sup>-2</sup> K<sup>-1</sup> at the across the width of the channel. The maximum values of  $h_{tp}(x, y)$  were calculated at the centre of the channel cross section at 10 mm from the channel entrance. The local enhancement of  $h_{tp}(x, y)$  possibly occurred as a result of departure of the non-spherical bubbles from the channel edges.

Figure 13 shows the evolution of the two-phase heat transfer coefficient  $h_{tp}(x,y)$  with time for  $G = 298 \text{ kg m}^{-2}\text{s}^{-1}$  and  $q = 179.2 \text{ kW m}^{-2}$ . The highest value of  $h_{tp}(x,y)$  was measured at the centre of the channel entrance. The flow visualisations revealed the simultaneous flow patterns presented in Figure 13 for  $t = 0.288 \text{ s}$ . The flow regime from 0 to 6-7 mm was observed to be bubbly flow. Small bubbles appeared to grow adjacent to both superheated channel edges. The nucleation sites were close to the channel entrance edges. The non-spherical shape of the bubbles, possibly resulted from the effect of the drag force on the bubble, during high mass flux conditions. At the channel entrance the heat transfer coefficient varied between 5,700 and 15,000 W m<sup>-2</sup> K<sup>-1</sup>. The bubbles were growing in size during their movement near the channel superheated walls. The bubbles later (from 9 to 14 mm) departed from the walls and they merged together, forming cap bubbles (curved tail) in different sizes that later formed slugs. Annular flow regime was dominant at the channel outlet (from 14 to 20 mm). Bubble growth in the liquid superheated layer between the vapour core and the walls resulted in entrainment of large droplets in the vapour annulus (Figure 13). The two-phase heat transfer coefficients reached their maximum values at the channel entrance.

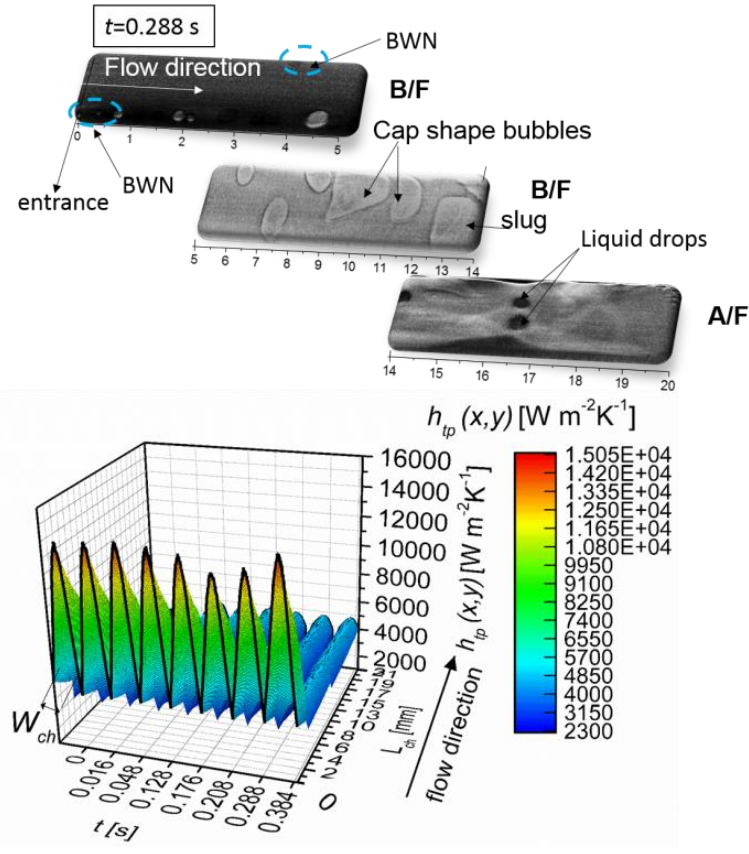


Figure 13. High spatial and temporal resolution 2D plot of  $h_{tp}(x, y)$  with time for the whole microchannel domain for  $G = 298 \text{ kg m}^{-2}\text{s}^{-1}$  and  $q = 179.2 \text{ kW m}^{-2}$  at  $t = 0.288\text{s}$ . The optical images on the top of the graph were simultaneously captured from the inlet, middle and outlet section of the microchannel and show the local flow patterns at each section.

### 4.3 BUBBLE DYNAMICS

The two-phase heat transfer coefficient 3D plots presented in Figures 8a, 8b, 9a, 12, and 13 revealed high heat transfer coefficients at the centre of the entrance of the channel width. From correlations of flow visualisations with Figure 8a from  $t = 0 \text{ s}$  to  $t = 0.170 \text{ s}$  the confined bubble across the depth and width of the channel across the entrance width was found to expand axially forming an elongated bubble. The enhancement of  $h_{tp}(x,y)$  occurred as a result of liquid film evaporation at the bubble base during the growth of the bubble along the channel axial direction.

Figure 14 demonstrates the effect of the confined bubble axial growth to the heat transfer coefficient at the channel base. The optical images were correlated with the contour plots of  $h_{tp}(x,y)$ . The two-phase heat transfer coefficient maximum value of  $4,860 \text{ W m}^{-2} \text{ K}^{-1}$  was measured at the centre of the bubble decreased with the axial growth of the bubble as more liquid possibly evaporates underneath the bubble. The maximum  $h_{tp}(x,y)$  was measured at the channel centre (entrance).

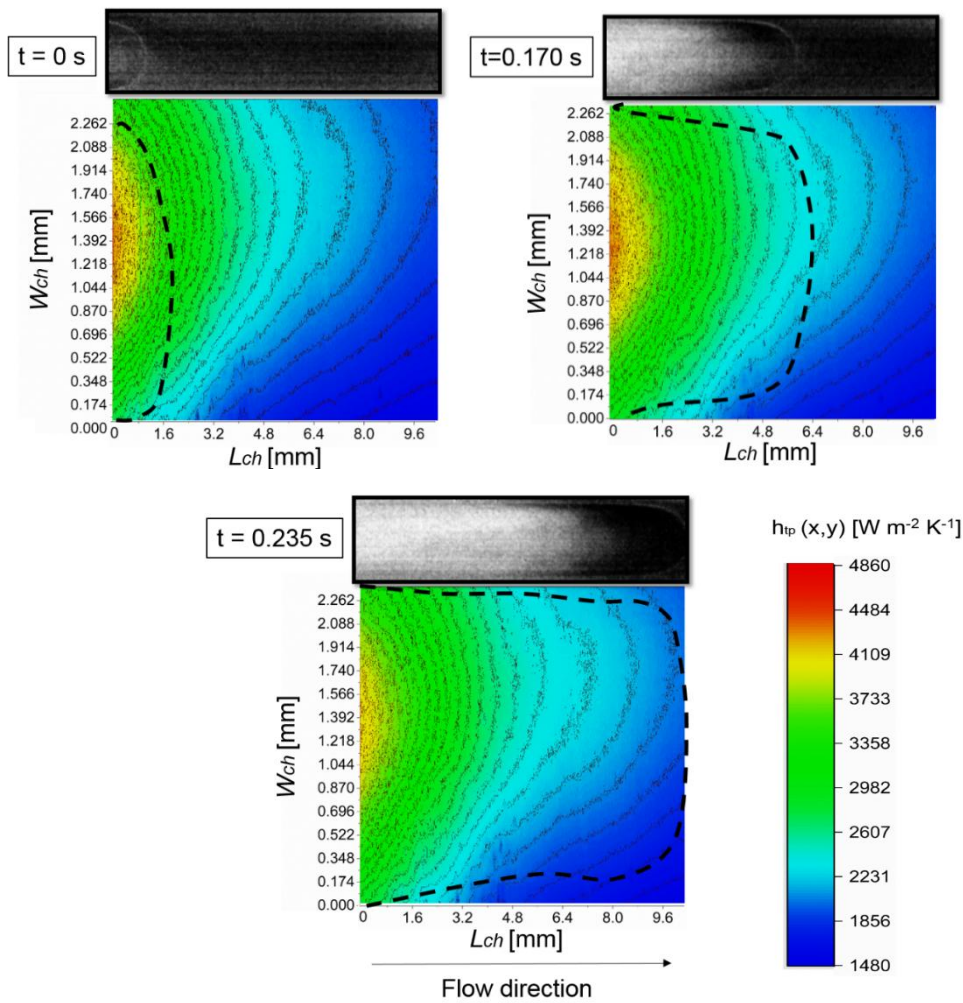


Figure 14. Effect of the confined bubble axial growth to the heat transfer coefficient at the channel entrance. Correlation between the optical images and the thermal images was achieved for the three time instances of  $t = 0 \text{ s}$ ,  $t = 0.170 \text{ s}$  and  $t = 0.235 \text{ s}$ .

At  $t = 0.235 \text{ s}$  instability in the curves was induced due to evaporation at the channel edges where the heat transfer coefficient was found to decrease  $2,231 \text{ W m}^{-2} \text{ K}^{-1}$ .

Figure 15 shows the  $h_{tp}(x,y)$  at a specific snapshot for the high mass flux of  $G = 298 \text{ kg m}^{-2}\text{s}^{-1}$  and heat flux of  $q = 179.2 \text{ kW m}^{-2}$ .  $h_{tp}(x,y)$  has a maximum value of  $5,040 \text{ W m}^{-2} \text{ K}^{-1}$  at centre of the channel width ( $x = 5 \text{ mm}$ ,  $y = 1.28 \text{ mm}$ ). However, the maximum value was transferred to the right of the channel edge ( $x = 14 \text{ mm}$ ,  $y = 1.60 \text{ mm}$ ) while moving to the outlet. This occurred due to the formation of large cap at the left side of the channel, resulting in non-uniform distribution of the two-phase heat transfer coefficient across the channel width.

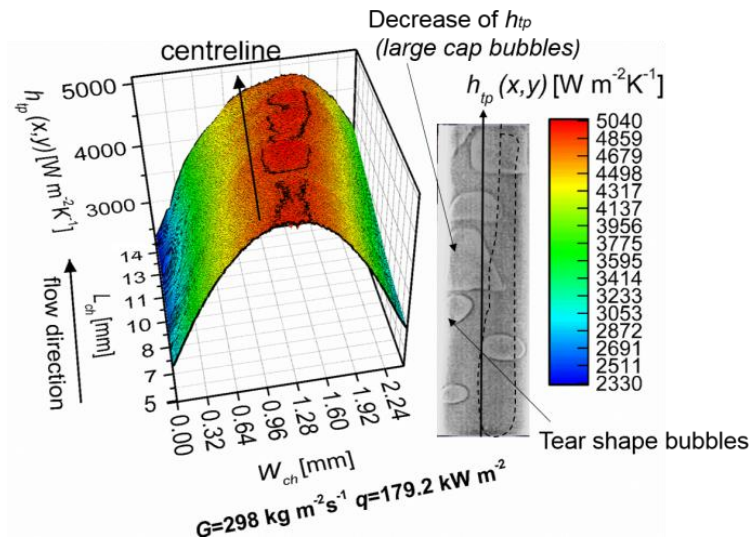


Figure. 15 Local two –phase heat transfer coefficient during bubbly flow from 5 to 14 mm along the channel for high mass flux of  $G = 298 \text{ kg m}^{-2}\text{s}^{-1}$  and  $q = 179.2 \text{ kW m}^{-2}$ . Correlation with simultaneous optical image of the same dimensions.

#### 4.4 PRESSURE FLUCTUATIONS

High heat transfer coefficients ( $1,100\text{-}16,000 \text{ W m}^{-2} \text{ K}^{-1}$ ) were obtained at low mass fluxes from  $7.37$  to  $11.47 \text{ kg m}^{-2}\text{s}^{-1}$ , with pressure drop values lower than  $75 \text{ mbar}$ .

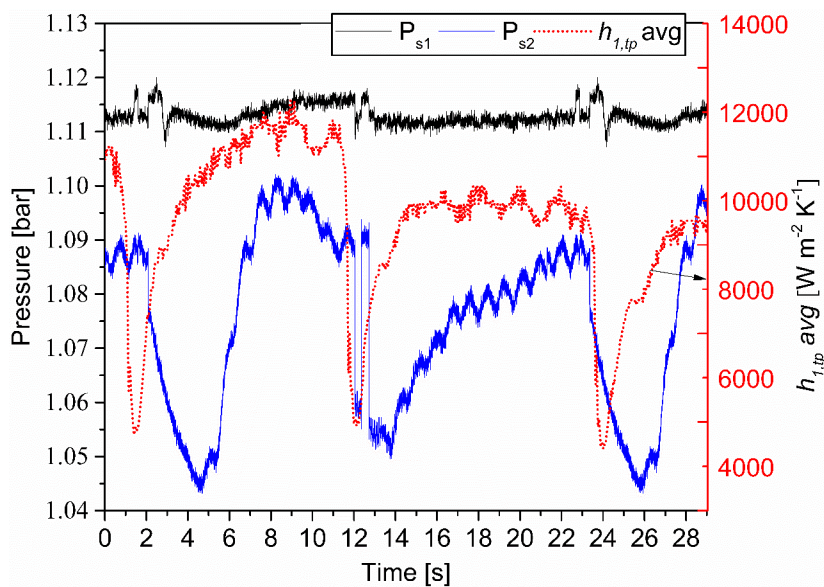


Figure 16. Two-phase pressure fluctuations at the inlet ( $P_{s1}$ ) and outlet ( $P_{s2}$ ) of the microchannel and the averaged locally two-phase hat transfer coefficient calculated at the channel inlet section for 29 s time interval at  $q = 30.97 \text{ kW m}^{-2}$  and  $G = 7.37 \text{ kg m}^{-2} \text{ s}^{-1}$ .

Pressure oscillations occurred as a result of bubble axial expansion that caused flow reversal in the channel. Flow reversal resulted in unstable flow mode with periodic pressure and wall temperature fluctuations. These temperature and pressure fluctuations resulted in periodic heat transfer coefficients fluctuations. Flow reversal occurred as a result of bubble expansion after bubble nucleation occurred at the channel entrance. Figure 16 shows that the pressure drop was periodically increased up to 75 mbar. This pressure drop increase was a result of the flow reversal induced by the axial expansion of the confined bubble along the microchannel. The two-phase heat transfer coefficient reached the maximum value of  $12,000 \text{ W m}^{-2}\text{K}^{-1}$  initially when the bubble was confined at the channel entrance and then decreased down to  $4,500 \text{ W m}^{-2}\text{K}^{-1}$  after bubble expansion that caused flow reversal [19] in the channel. Kandlikar [19] reported that the location of nucleation can affect the flow instabilities. When bubble nucleation is observed to occur at the channel inlet, the flow resistance in the backflow direction decreases and thus flow reversal occurs. During the high amplitude fluctuations at low mass fluxes bubble nucleation and confined growth occurred at the channel entrance inducing high pressure drop as a result of the blockage of liquid flow in the channel.

## 5. CONCLUSIONS

The simultaneous recordings of high spatial and temporal resolution thermal images and optical images with local pressure drop assisted in a better understanding of the heat transfer coefficient and liquid-vapour distribution of the microchannel surface. Local heat transfer coefficients were correlated with the contrast of the high quality optical images. The effect of the local flow patterns on the two-dimensional two-phase heat transfer coefficient was studied with special attention on flow instability cycles. The results revealed local enhancement of the heat transfer coefficient at the centre of the channel entrance. The maximum heat transfer coefficient occurred before axial expansion of the fully confined bubble at the channel entrance for low mass fluxes and heat fluxes ( $< 45 \text{ kW m}^{-2}$ ). However the axial expansion of the elongated confined bubble along the whole channel domain assisted in flow reversal, suspected dryout at the channel edges and high amplitude temperature and pressure fluctuations. The wall temperature appeared non-uniform during boiling across the channel domain. The 3D two-phase heat transfer coefficient plots revealed details

about the locations of heat transfer enhancement and deterioration. The high spatial resolution of the heat transfer coefficient data revealed dips and peaks at the centre of the channel for high mass fluxes and where correlated with optical images that reveal the local flow regimes. The  $h_{tp(x,y)}$  varied significantly across the channel width. The heat transfer coefficient profile across the channel section peaked at the centre of the entrance in all the examined cases. This occurred mainly at the entrance of the channel just before the axial expansion of a confined bubble for low mass fluxes. However, moving from the bubbly flow regime to the slug-annular flow regime at the peak of the profile moved closer to one corner of the channel because of the presence of large bubbles that caused probably deterioration of the heat transfer. As a result, the heat transfer coefficient profile at the channel cross section was found non uniform along the whole channel domain. The contrast of the optical images revealed the vapour-liquid interface during bubble confinement, slug and annular flow regime. Annular flow was the main flow regime observed to occur at high heat fluxes ( $> 45 \text{ kW m}^{-2}$ ), with film boiling and entrainment of liquid drops in the vapour annulus that caused suspected dryout at the base. The effect of the confined bubble axial growth to the two-phase heat transfer coefficient distribution at the channel entrance was also studied at low mass fluxes and low heat fluxes. The high amplitude fluctuations of the local heat transfer coefficient were related with the axial growth of the confined to channel width bubble from the channel entrance along the whole length of the channel.

## ACKNOWLEDGMENTS

The authors thank the Engineering and Physical Sciences Research Council (EPSRC) through a research grant (EP/K00963X/I) and SK acknowledges financial support from EPSRC through a DTA grant.

## REFERENCES

1. Karayiannis, T.G. and M.M. Mahmoud, *Flow boiling in microchannels: Fundamentals and applications*. Applied Thermal Engineering, 2017. **115**: p. 1372-1397.
2. Jinliang, X., et al., *Microscale boiling heat transfer in a micro-timescale at high heat fluxes*. Journal of Micromechanics and Microengineering, 2005. **15**(2): p. 362.
3. Chen, J.C., *Correlation for Boiling Heat Transfer to Saturated Fluids in Convective Flow*. Industrial & Engineering Chemistry Process Design and Development, 1966. **5**(3): p. 322-329.
4. Gan, Y., J. Xu, and S. Wang, *Are the available boiling heat transfer*

- coefficients suitable for silicon microchannel heat sinks?* Microfluidics and Nanofluidics, 2008. **4**(6): p. 575-587.
5. Gungor, K.E. and R.H.S. Winterton, *A general correlation for flow boiling in tubes and annuli*. International Journal of Heat and Mass Transfer, 1986. **29**(3): p. 351-358.
  6. Kandlikar, S.G., *A General Correlation for Saturated Two-Phase Flow Boiling Heat Transfer Inside Horizontal and Vertical Tubes*. Journal of Heat Transfer, 1990. **112**(1): p. 219-228.
  7. Liu, Z. and R.H.S. Winterton, *A general correlation for saturated and subcooled flow boiling in tubes and annuli, based on a nucleate pool boiling equation*. International Journal of Heat and Mass Transfer, 1991. **34**(11): p. 2759-2766.
  8. Steiner, D. and J. Taborek, *Flow Boiling Heat Transfer in Vertical Tubes Correlated by an Asymptotic Model*. Heat Transfer Engineering, 1992. **13**(2): p. 43-69.
  9. Tran, T.N., M.W. Wambsganss, and D.M. France, *Small circular- and rectangular-channel boiling with two refrigerants*. International Journal of Multiphase Flow, 1996. **22**(3): p. 485-498.
  10. Warriar, G.R., V.K. Dhir, and L.A. Momoda, *Heat transfer and pressure drop in narrow rectangular channels*. Experimental Thermal and Fluid Science, 2002. **26**(1): p. 53-64.
  11. Xu, J.L. and Y.H. Gan, *Uniform Membrane Chip Temperatures in the Nucleate Boiling Heat Transfer Region by Selecting Suitable, Medium Boiling Number Range*. Nanoscale and Microscale Thermophysical Engineering, 2007. **11**(3-4): p. 273-300.
  12. Hapke, I., H. Boye, and J. Schmidt, *FLOW BOILING OF WATER AND n - HEPTANE IN MICRO CHANNELS*. Microscale Thermophysical Engineering, 2002. **6**(2): p. 99-115.
  13. Krebs, D., et al., *Spatially resolved wall temperature measurements during flow boiling in microchannels*. Experimental Thermal and Fluid Science, 2010. **34**(4): p. 434-445.
  14. Liu, T.-L. and C. Pan, *Infrared thermography measurement of two-phase boiling flow heat transfer in a microchannel*. Applied Thermal Engineering, 2016. **94**: p. 568-578.
  15. Gan, Y., J. Xu, and Y. Yan, *An experimental study of two-phase pressure drop of acetone in triangular silicon micro-channels*. Applied Thermal Engineering, 2015. **80**: p. 76-86.
  16. Xiong, L.C., P. Chen, and Q.S. Zhou, *Adhesion promotion between PDMS and glass by oxygen plasma pre-treatment*. Journal of Adhesion Science and Technology, 2014. **28**(11): p. 1046-1054.
  17. P. Madding, R., *Emissivity measurement and temperature correction accuracy considerations*. Vol. 3700. 1999.
  18. Drew, T.B., H.C. Hottel, and W.H. McAdams, *Heat transmission*. Transactions of the American Institute of Chemical Engineers, 1936. **32**: p. 271-305.
  19. Kandlikar, S.G., *Nucleation characteristics and stability considerations during flow boiling in microchannels*. Experimental Thermal and Fluid Science, 2006. **30**(5): p. 441-447.